Two-Element Optical Array Receiver Field Demonstration

V. Vilnrotter,[1] C.-W. Lau,[1] K. Andrews,[1] P. Vo,[1] M. Srinivasan,[1] and D. Lee[1]

The results of field experiments designed to demonstrate key enabling concepts of optical array receivers are presented in a field environment similar to actual operating conditions. The theoretical framework and analytical evaluation of optical array receivers have been developed and documented in previous articles [1,4]. This article describes the implementation and field evaluation of a two-element optical array receiver incorporating photon-counting, signal conditioning, high-speed digital sample distribution, adaptive delay compensation, and sample combining operations required for array reception of intensity-modulated optical pulse-position modulated (PPM) signals. Data collected in the field were processed off-line to determine communications performance of a two-element optical array and to demonstrate the inherent advantages of optical array reception.

I. Introduction

A stated objective of future deep-space missions is to dramatically increase the useful data rate, thus achieving greater science data return for each mission. This goal can be accomplished effectively through the use of optical rather than radio frequency wavelengths. Due to cost and complexity considerations, the most practical approach at optical wavelengths is to employ a ground-based receiver, designed to mitigate the effects of atmospheric turbulence for best performance. A novel approach for ground-based optical communications is the concept of synthesizing a large optical aperture by means of an array of smaller telescopes, each containing a properly designed focal-plane array to reduce losses due to turbulence. Based on theoretical considerations and preliminary experimental results to date, the optical array receiver approach appears to be a viable and robust alternative to single large-aperture optical receivers.

In addition to the theoretical feasibility of array reception as described in [1], array receivers offer additional advantages over single-aperture receivers for ground-based reception of optical signals, including graceful performance degradation in case of telescope failure, ease of future expansion to increase throughput or extend communications range, relaxed performance requirements on telescopes, and reduced implementation cost. The theoretical equivalence of the array receiver and the single large telescope receiver under operating conditions of interest has been shown in [1], and results of initial field experiments were reported in [2,3]. In this article, we present the results of field experiments carried out with

a two-element optical array in order to demonstrate communications performance gain and evaluate the feasibility of employing cost-effective telescopes in future optical array receivers.

II. System Description

The third and final year of this research and technology development (R&TD) effort focused on extending the theoretical investigations and preliminary field demonstrations of the first two years to real-time detection and sampling and delay compensation of pulsed-laser modulation, as well as on a realistic, operational-like demonstration of acquisition and tracking of stellar sources. This effort required the implementation of a real-time high-data-rate signal processing assembly at each telescope that converted the output pulses of the detector elements into four-bit numbers and generated samples for transmission to an adaptive digital delay-compensation and combining assembly designed specifically for pulsed signals such as pulse-position modulation (PPM). The aligned samples were summed in real time to produce array output samples that were recorded in the field and processed off-line using a software receiver to establish array performance and gain.

A. Optical Array Receiver

A conceptual block diagram of an optical array receiver suitable for long-range free-space communication is shown in Fig. 1. The most conspicuous feature of an optical array receiver is a large number of small- to medium-sized telescopes, with apertures and the number of telescopes designed to synthesize the total desired collecting area. This array of telescopes is envisioned as being fully computer-controlled via a user interface and predict-driven to achieve rough pointing and tracking of the desired source. Fine-pointing and tracking functions then take over to keep each telescope pointed towards the source despite imperfect pointing predicts, telescope drive errors, and disturbances caused by wind.

The optical signal collected by each telescope is focused onto a photon-counting Geiger avalanche photodiode (GAPD) detector array located in the focal plane, designated the focal-plane array (FPA). Despite atmospheric turbulence degrading the coherence of the received signal fields and interfering
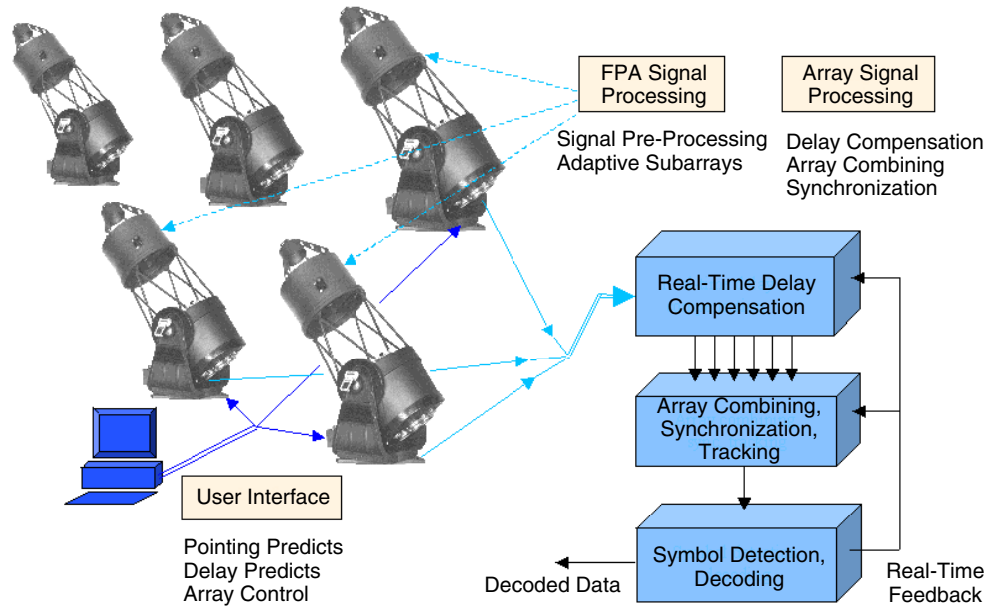

Fig. 1. A conceptual design of an optical array receiver, illustrating key functions required for optical array reception. The picture of the 63.5-cm telescopes is courtesy of JMI Telescopes, Colorado.

background radiation within the passband of the optical pre-detection filter, the FPA and associated digital signal-processing electronics extracts real-time pointing information and keeps the centroid of the signal distribution centered over the FPA. This can be accomplished in two steps: First, large accumulated pointing errors are fed back to the telescope drive assembly, re-pointing the entire telescope; and second, small excursions of the signal distribution from the center of the FPA are corrected via a fast-response tip–tilt mirror that responds to real-time pointing updates generated by the FPA electronics. In addition, the short-term average signal energy over each detector element can be measured and used to implement adaptive background-suppression algorithms to improve or optimize the communications performance of the entire array.

The electrical signals generated at each telescope by the FPA signal-processing assembly are collected at a central array processing station, where the final operations necessary for data detection and decoding are carried out. The relative time delay between signals from various telescopes is measured and removed, effectively aligning each signal stream in time before further processing is carried out. The delay-compensated signals then are combined to optimize array performance and are further processed to enable symbol synchronization, frame synchronization, and tracking in order to maintain lock between the combined signal and the receiver time frame. Following synchronization, the received and combined channel symbols are detected using a maximum-likelihood decision strategy. If encoded, the detected channel symbols (or other appropriate decision statistics) then would be handed over to a decoder, further improving upon the bit-error probabilities of the uncoded symbols. The channel symbols detected by the array receiver also can be used by the array processing assembly to further aid the delay compensation, array combining, and synchronization operations.

B. High-Speed Digital Electronics

A block diagram of the two-element optical array communications electronics assembly (OACEA) is shown in Fig. 2, including the high-speed FPA, signal conditioning electronics, adaptive delay compensation and combining assembly, and digital receiver. With the exception of the digital receiver, all functional blocks have been implemented in high-speed digital electronics, tested, and used to perform communications experiments in the field.
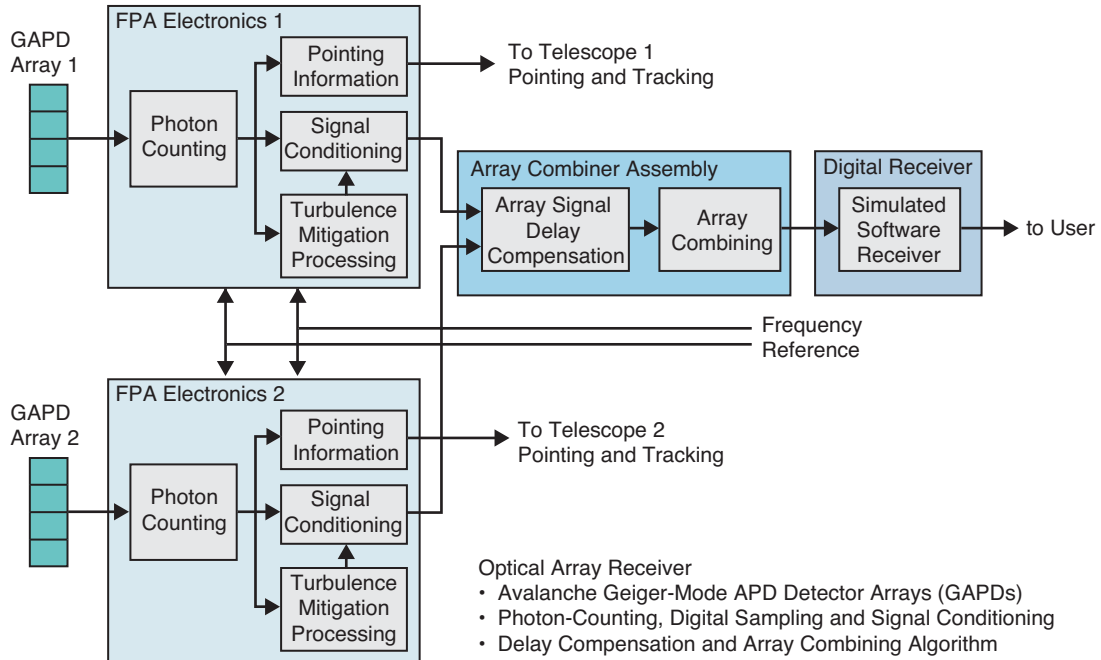

Fig. 2. Functional block diagram of high-speed, digital array electronics.

3

1. High-Speed Focal-Plane Assembly. The functions of the FPA assembly are to process the digital pulses from the GAPD arrays into samples, derive pointing information to refine the telescope pointing in real time, and produce real-time detector masks for turbulence mitigation. A picture of the high-speed field programmable gate array (FPGA) board designed to process the photon-response pulses generated by the GAPD detector array in conjunction with an active quenching circuit (AQC) array (developed by aPeak Inc.) is shown in Fig. 3(a), along with a typical photon response of a GAPD-plus-AQC detector element in Fig. 3(b). An off-the-shelf microlens array was integrated into the GAPD array with the role of increasing the fill factor to more than 90 percent and focusing the received optical field onto the detector elements. Additional functions carried out by this design include telescope auto-guiding and automatic mask generation to reduce background interference while collecting most of the signal energy, when operating in turbulence.

Each telescope is equipped with a GAPD photon-counting detector array with 16 detector elements arranged on a square grid, with 200 μm pitch, integrated into the detection module with a 16 element AQC array. The FPA array processor is comprised of a Xilinx Spartan XC3S200 FPGA on a Digilent commercial off-the-shelf (COTS) circuit board mounted on a Zilog eZ80F91 COTS circuit board. The Xilinx FPGA logic, developed in Verilog, handles the real-time data processing whereas the Zilog micro-controller software, developed in C, provides the user interface. The Zilog microcontroller board facilitates user programmability of embedded FPGA registers, such as integration time and masking controls, as well as a diagnostic capability, allowing the user read access to internal data registers, through a simple serial cable connection to a PC. The FPGA sampling assembly detects the leading edge of each pulse from every detector element and produces a 4-bit sample every 8 ns, thus producing samples at a rate of 125 million samples per second.

2. Adaptive Delay Compensation and Combining Assembly. The adaptive delay compensation and combining assembly (ADCCA) functions are carried out in the array signal-processing assembly. A block diagram of this design, considerably simplified from the previous design described in [4] in order to facilitate digital implementation, is shown in Fig. 4. Samples from the FPA electronics assembly are transmitted in a low-voltage differential signaling (LVDS) format over a pair of 10-meter cables to the ADCCA. The primary function of the simplified ADCCA is to sense and correct for delay drifts between
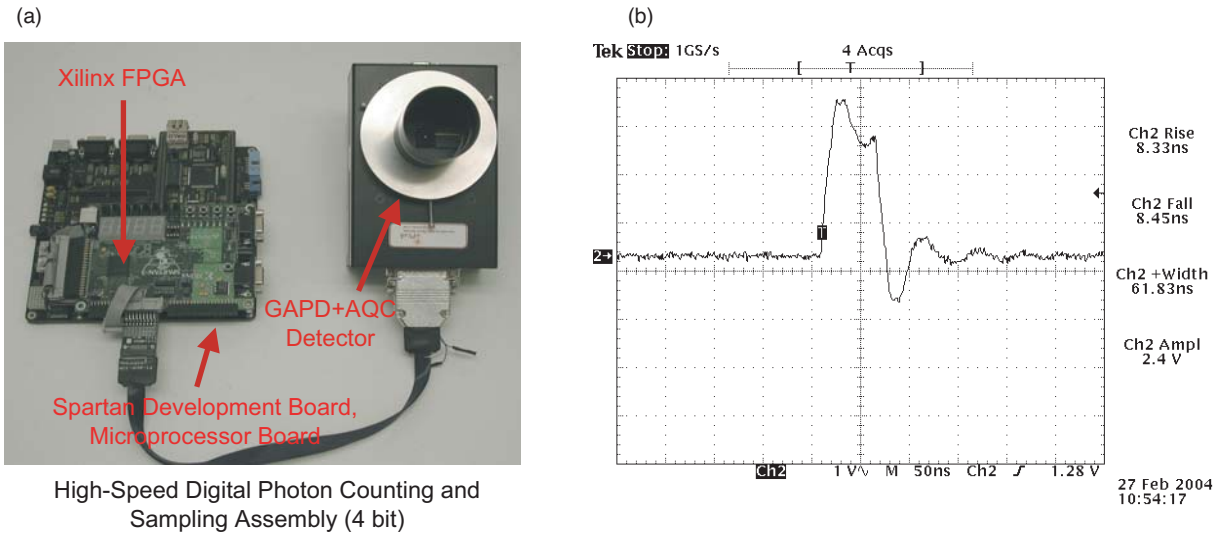

Fig. 3. High-speed focal-plane detector assembly: (a) photon-counting GAPD+AQC detector array module (aPeak, Inc.) connected to the FPA array processor and (b) electrical response of the GAPD+AQC array detector module to single photons (laboratory data).
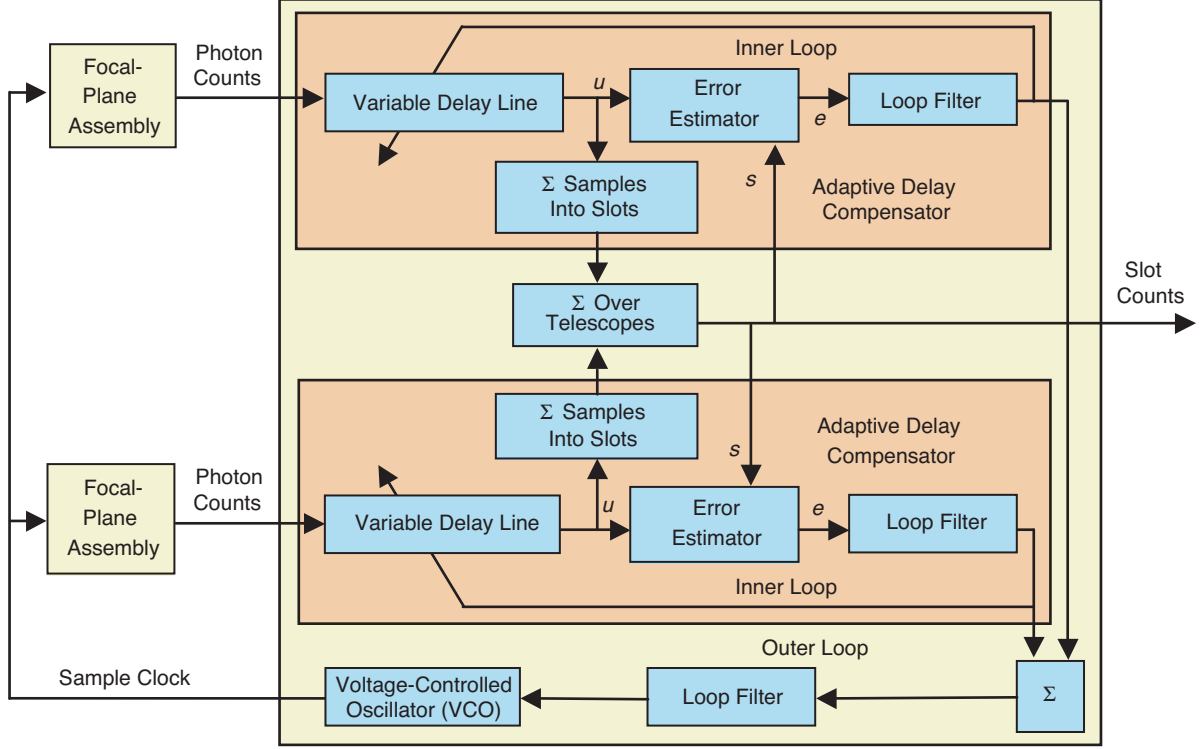
Fig. 4 Functional block diagram of the simplified delay compensation and combining assembly (ADCCA).

the telescopes, thus maximizing the signal-generated photon counts in the combined PPM pulses. The digital hardware employed in this design also uses a Xilinx Spartan XC3S200 FPGA on a Digilent COTS circuit board, and the logic was again developed in Verilog.

The delay compensator uses a blind adaptive decision-feedback algorithm, motivated by the least-mean square (LMS) algorithm [5]. To justify our design, we briefly review LMS adaptive equalization, which is a discrete-time algorithm. Suppose the transmitted sequence of symbols s_i, for $0 \leq i \leq T - 1$, is received as a sequence of vectors $\mathbf{y}_i$, after channel distortion, perhaps including the addition of noise, fading, inter-symbol interference (ISI), or fractionally spaced sampling.

The receiver attempts to compute an approximation $\hat{s}_i$ of s_i as $\hat{s}_i = \mathbf{y}_i \cdot \mathbf{w}$, by judicious choice of the vector $\mathbf{w}$. The receiver does this by attempting to minimize a cost function defined as the mean of the instantaneous squared errors $c_i = (\hat{s}_i - s_i)^2$:

$$C(\mathbf{w}) = \frac{1}{T} \sum_{i=0}^{T-1} c_i = \frac{1}{T} \sum_{i=0}^{T-1} (\hat{s}_i - s_i)^2 = \frac{1}{T} \sum_{i=0}^{T-1} (\mathbf{y}_i \cdot \mathbf{w} - s_i)^2$$

The minimum cost occurs for $\mathbf{w}$ such that $\nabla_w C(\mathbf{w}) = \mathbf{0}$, and LMS attempts to find this optimal choice of $\mathbf{w}$ iteratively through gradient descent on the instantaneous cost:

$$\mathbf{w}_{i+1} = \mathbf{w}_i - \mu \mathbf{e}_i$$

where

$$\mathbf{e}_i = \nabla_w c_i = \nabla_w (\mathbf{y}_i \cdot \mathbf{w}_i - s_i)^2 = 2(\mathbf{y}_i \cdot \mathbf{w}_i - s_i)\mathbf{y}_i$$

and μ is a small constant that determines the convergence rate. Note that the computation of $\mathbf{e}_i$ requires knowledge of s_i, either as a training signal or through decision feedback.

Our delay compensation algorithm has a structure similar to the LMS algorithm, although the cost function is very different and is derived in continuous time. Let t be time measured in units of slot durations, so the transmitter sends a continuous-time signal $s(t)$ that is a sum of unit pulses,

$$s(t) = \sum_{i=0}^{T-1} s_i p(t - i)$$

where $p(t) = 1$ for $0 \leq t < 1$ and is zero otherwise. Let $\mathbf{y}(t)$ be a (continuous-time) N-dimensional vector-valued function with one component $y_n(t)$ per telescope, each of which consists of a string of delta functions representing photon detection events. That is, $y_n(t) = \sum_{k=1}^{K_n} \delta(t - t_n(k))$, where $t_n(k)$ is the time at which the nth telescope receives its kth photon. The receiver attempts to construct synchronized versions of the received telescope signals, $u_n(t) = y_n(t - \tau_n)$, by finding an appropriate N-dimensional vector of delays $\boldsymbol{\tau}$ (each component of which is potentially negative). Their sum, $\hat{s}(t)$, then will be an approximation of the transmitted signal $s(t)$,

$$\hat{s}(t) = \sum_{n=1}^{N} u_n(t) = \sum_{n=1}^{N} y_n(t - \tau_n)$$

The receiver algorithm is derived by *maximizing* the cost function defined as the correlation,

$$C(\boldsymbol{\tau}) = \frac{1}{T} \int_0^T s(t)\hat{s}(t)\, dt$$

$$= \frac{1}{T} \int_0^T \sum_{n=1}^{N} s(t) y_n(t - \tau_n)\, dt$$

$$= \frac{1}{T} \sum_{n=1}^{N} \sum_{i=0}^{T-1} \int_i^{i+1} s(t) y_n(t - \tau_n)\, dt$$

$$= \frac{1}{T} \sum_{i=0}^{T-1} c_i$$

where $c_i = \sum_{n=1}^{N} \int_i^{i+1} s(t) y_n(t - \tau_n)\, dt$ is the slot-by-slot cost. The maximum occurs when $\nabla_\tau C(\boldsymbol{\tau}) = \mathbf{0}$, and, again, our algorithm attempts to find this value of $\boldsymbol{\tau}$ iteratively, based on the gradient of this sample-by-sample cost, $\mathbf{e}_i = \nabla_\tau c_i$. This can be computed component-wise:

$$e_{n,i} = \frac{\partial}{\partial \tau_n} \left(\int_i^{i+1} s(t) y_n(t - \tau_n)\, dt \right)$$

Because $s(t)$ has the constant value s_i over this interval,

$$e_{n,i} = s_i \frac{\partial}{\partial \tau_n} \left(\int_i^{i+1} y_n(t - \tau_n)\, dt \right)$$

$$= s_i \big(y_n(i - \tau_n) - y_n(i + 1 - \tau_n) \big)$$

$$= s_i \big(u_n(i) - u_n(i + 1) \big) \tag{1}$$

This error function cannot be computed in practice because the instantaneous values $u_n(i)$ and $u_n(i+1)$ are not physically meaningful (recall $u_n(t)$ is a sequence of delta functions).

In practice, the delay compensation algorithm is implemented in discrete time, updated at a sample rate that is K times the slot rate. Rather than a sequence of delta functions, the nth telescope generates observations $y_{n,Ki+j}$ representing the number of photons detected during the jth sampling interval of the ith slot, $0 \leq j < K$. We constrain each delay τ_n to integral multiples of $1/K$, so $u_{n,Ki+j} = y_{n,Ki+j-K\tau_n}$ is also a discrete-time signal, updated synchronously with $y_{n,Ki+j}$.

In Eq. (1), the instantaneous values $u_n(i)$ and $u_n(i+1)$ must each be approximated by the immediately preceding or the immediately following sample. We use $u_n(i) \approx u_{n,Ki-1}$ and $u_n(i+1) \approx u_{n,K(i+1)}$ for the increased capture range these choices provide.

Equation (1) also assumes knowledge of the transmitted pulse sequence s_i. To construct a blind algorithm, i.e., one that need not know the transmitted signal, we use decision feedback and replace s_i with the receiver's estimate, $\hat{s}_i$. We assume that a priori delay estimates are sufficient for capture and pull-in to occur, or that capture can be induced by sweeping the element delays with respect to each other.

In summary, our adaptive delay compensation algorithm is

$$u_{n,Ki+j} = y_{n,Ki+j-K\tau_{n,i}}$$

$$\hat{s}_i = \sum_{n=1}^{N} \sum_{j=0}^{K-1} u_{n,Ki+j}$$

$$e_{n,i} = \hat{s}_i \big(u_{n,Ki-1} - u_{n,K(i+1)} \big)$$

$$\tau_{n,i+1} = \tau_{n,i} - \mu e_{n,i}$$

where each $\tau_{n,i}$ is constrained to be an integral multiple of $1/K$. Note that each y_n and u_n runs at the faster sample rate, and the other signals run at the slower slot rate. A block diagram of the circuit that performs these functions is shown in Fig. 4.

With an adaptive delay compensation estimator for each element of the array, there is nothing that matches the receiver's sample rate to that of the received signal. If these were to deviate for long, each array element's delay line could overflow or underflow. To prevent this, the delay compensation algorithm includes an outer rate-compensating feedback loop that adjusts the receiver's master sample clock so that the average fullness of the delay lines stays within physical limits.

Currently, the loop filters are simple accumulators; hence, they do not maintain constant loop bandwidth as signal amplitude and loop gain vary. The error estimator performs blind slot-timing recovery and helps maintain sharp slot boundaries in the combined signal by adjusting the delay of the two input streams relative to each other, thus keeping the received pulses from the two telescopes synchronized.

Before proceeding with the hardware implementation, baseline performance of the simplified delay compensation loop was established through simulation. An example of a simulation output demonstrating compensation for an initial delay offset is shown in Fig. 5, where an initial delay offset of eight samples was applied between the two sample streams.

The combined output of the pulse slots is seen to increase rapidly, while the error signal decreases simultaneously, reaching steady-state tracking in approximately 900 slot durations. At high data rates, this typically corresponds to a fraction of a millisecond and should be more than adequate to track slow changes in delay due to array–spacecraft geometry during an operational pass. A picture of the complete OACEA assembly, before installation on the telescopes, is shown in Fig. 6.

C. Daytime Acquisition and Tracking Experiments

Each telescope of an optical array receiver must be able to acquire and track the desired source, based on predicted ephemerides supplied by a central control computer, and to provide accurate and repeatable mechanical alignment of the telescope axes. Conceptually, the key operations required for successful acquisition and tracking consist of establishing the relationship between the telescope mechanical coordinates and the celestial coordinates, learning and modeling the coordinate-dependent distortion vector for each telescope, obtaining time-tagged spacecraft coordinates with a degree of accuracy consistent with the acquisition camera's field of view (FOV), and, finally, refining the telescope pointing to initiate tracking with the high-speed and narrow FOV photon-counting detector array used for communications. Research-grade computer-controlled telescopes manufactured today having optics within the range of 1/2 to 1 meter in diameter are capable of carrying out these operations with sufficient accuracy and precision. However, the cost of mechanical mounts and gear assemblies for large-aperture telescopes tends to be
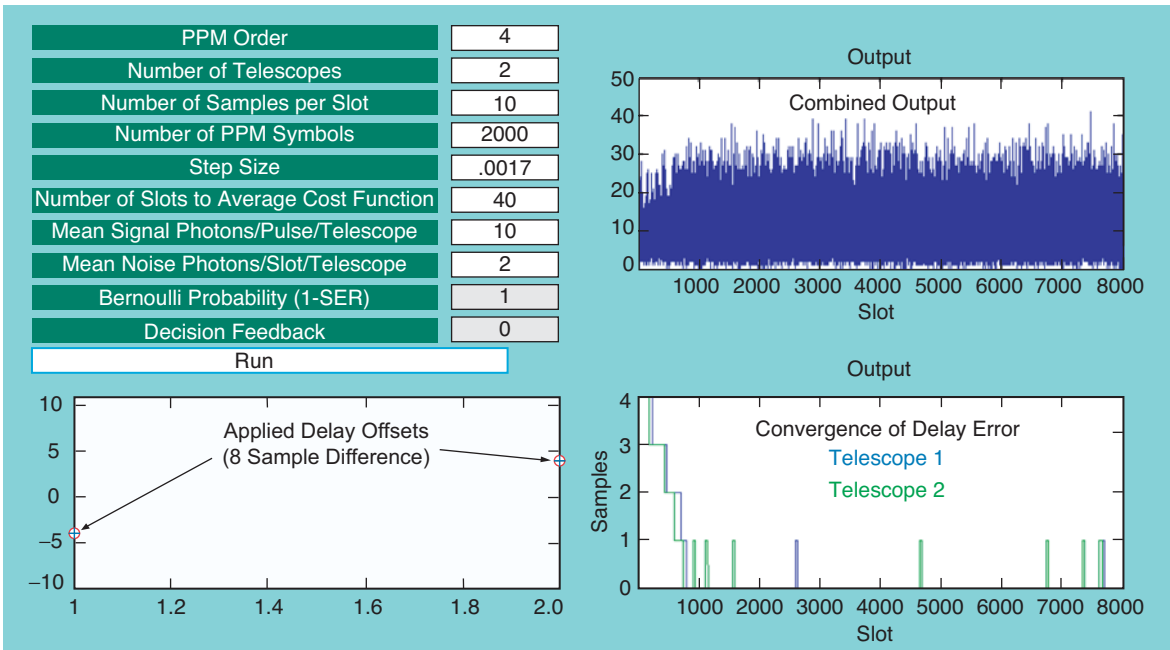

Fig. 5. Simulated performance of the simplified digital delay compensation algorithm in strong background (10 signal photons per slot, 2 background photons per slot, 4 PPM, stepsize = 0.0017).

Fig. 6. Complete OACEA, before installation on 63.5-cm telescopes, including aPeak detector modules, focal-plane electronics, high-speed 4-bit LVDS cable assemblies, and adaptive delay compensation and combining board.

excessive for array applications, where typically a large number of telescopes are required. Therefore, it was our intent to address these requirements using cost-effective 63.5-cm telescopes manufactured for the amateur market and to evaluate their performance as related to future optical array receiver applications.

Acquisition and tracking experiments were carried out in May and June 2005 on the JPL Mesa antenna test range. The 63.5-cm telescopes were found to have excellent diffraction-limited optics, and the computer-controlled drive assemblies with "go-to" capability facilitated acquisition of bright reference stars. Since future optical array receivers will have to be operational during the day, when acquisition and tracking is much more challenging than at night due to greatly increased background radiation, these tracking experiments were carried out both at night and during the day (special tents were procured to shade the equipment from the Sun for daytime operation). Daytime acquisition and tracking experiments relied on a state-of-the-art, high-sensitivity wide-field digital charge-coupled device (CCD) camera called the Trifid, manufactured by Yankee Robotics, Inc., of California. The camera was customized by removing the infrared (IR)-opaque protective window and replacing it with a 1-nm bandwidth optical filter centered at 1064 nm, one of the wavelengths considered likely to be employed in future deep-space optical communications. New software was developed and installed to enable high-speed imaging and downloading, enabling the camera to produce a continuous stream of 1-s exposures followed by 400-ms download intervals, for hours at a time. The downloaded images were time-tagged using the computer's internal clock, which in turn was synchronized to an accurate reference clock. This configuration and methodology could be employed in the future to identify and center the spacecraft source.

The mean value of the background-generated counts in each pixel through a 1-nm optical filter centered at 1064 nm varied from a few thousand per second under clear skies to tens of thousands per second during bright, hazy conditions. It was found that the full-well capacity of the camera (approximately 60,000 detected photons) was never exceeded with this design, even when pointing the telescopes to within a few degrees of the Sun. Since the average background level can be subtracted from each pixel, only the variation introduced by the background photons impedes signal detection. The Poisson process is a good theoretical model for multimode background radiation: For Poisson-distributed random variables, the standard deviation is proportional to the square root of the mean; therefore, tens of thousands of background counts generate an intensity variation of only several hundred photons. This implies that during high-data-rate communications, designed to deliver one or more detected photons per pulse to the array in order to maintain the desired communications performance, the signal count over a nominal 1-s

integration with a comparable widefield digital camera would easily exceed the background interference at each telescope. For example, a PPM symbol rate of 1 megasample per second would deliver several million signal photons to the array each second: Even if the array consisted of a thousand telescopes, each telescope would observe an average of thousands of signal photons every second, enabling acquisition and tracking of the source by each telescope of the array.

During field experiments, the widefield Trifid camera provided clear images of Venus only a few degrees from the Sun and of Sirius at low elevation through bright haze. The images of Venus and Sirius obtained with the Trifid camera are shown in Fig. 7. These images were obtained using "star-hopping," where a relatively bright reference object such as Mars was initially centered in the field of view of the camera, then the coordinates of the next object were entered into the computer, and the telescope was commanded to these new coordinates. In each case, the subsequent target appeared in the FOV of the camera, generally off-center by less than 1/4 deg. These experiments confirmed the blind-pointing capability of the telescopes to be approximately 1/4 deg, which is adequate for acquisition and automated recognition of optical targets in an operational array tracking scenario. However, due to small residual backlash in the gear assembly even after backlash compensation has been applied (which is inconsequential for amateur star gazing but might impact autonomous array receiver operation), special care had to be exercised to develop the initial star model the computer employs to "go-to" each selected target. As such, the reference stars had to be selected so as not to reverse the motors during the initial calibration process or during subsequent tracking. Since the tracking of deep-space sources was mostly sidereal, the entire calibration was conducted in the clock-wise direction. With this method, it was possible to obtain 1/4-deg go-to accuracy during subsequent acquisition and tracking experiments.

D. Field Demonstration of Array Combining Using PPM Symbols

Optical communications field experiments were carried out on the JPL Mesa antenna test range in August and September 2005. These pulsed-laser communications experiments employed pulse-position-modulated (PPM) laser signals in a field environment that produced turbulence and was subject to wind and thermal effects. Both telescopes were equipped with field versions of the high-speed photon-counting detector arrays, the complete OACEA, and custom-built cables capable of carrying 8-ns 4-bit samples approximately 10 meters to the digital combining assembly.

The pulsed-laser communications experiments took place on the north-facing part of the mesa, as shown in Fig. 8, with the telescopes facing towards the San Gabriel Mountains. The laser transmitter consisted of a 635-nm laser, a 20× microscope objective to increase beam divergence, and a PPM modulation assembly. The original intent was to demonstrate high-speed communications using 8-ns pulses, and,
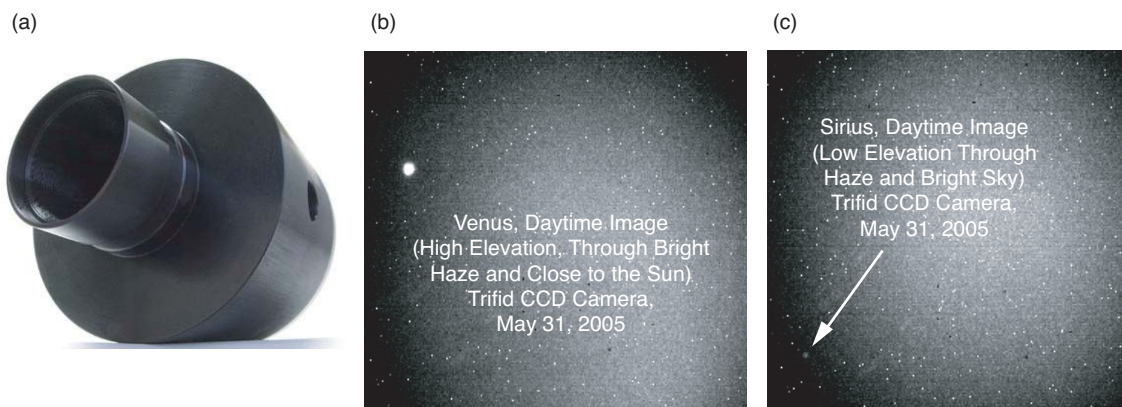
(a) (b) (c)

Fig. 7. Wide-field CCD camera used in daytime imaging experiments: (a) customized Yankee Robotics Trifid camera used in daytime acquisition experiments, and daytime images of (b) Venus and (c) Sirius obtained under bright hazy conditions.

Fig. 8. Experimental setup on the JPL Mesa test range, for reception of PPM signals.

indeed, high-speed lasers capable of generating nanosecond pulses were procured (operating at 765-nm wavelength). However, the interface between the high-speed lasers and the modulator could not be fully established in time for these experiments. It was decided to lower the clock rate of the digital assemblies to 25 MHz, generating 40-ns samples, and to use the slower 635-nm laser as the transmitter to generate 64PPM signals with 1-μs pulses. In addition, the road to the remote transmitter facility was damaged by rain, making it impractical to set up the transmitter assembly at the remote site. Therefore, these initial laser communications experiments took place across the parking lot at an approximate distance of 60 m. The experiments were carried out at night to reduce background interference, and they consisted of either repetitive 1-μs pulses or modulated 64PPM laser signals. The beam was expanded sufficiently to encompass both telescopes, and neutral density filters were used at the transmitter to further reduce signal strength at the array receiver. Calculated values for average detected photons per pulse expected at each telescope, taking into account geometry, vignetting, and detector efficiency, were consistent with the experimentally measured photon counts.

E. Detection Performance of the Two-Element Optical Array Receiver

The telescopes were roughly equally distant from the transmitter during these experiments; therefore, it was not practical to generate large enough delays between the telescopes to evaluate the performance of the ADCCA with the current experimental configuration. However, both individual and summed slot counts from the combiner were analyzed in detail and found to be consistent. A portable logic analyzer was used to record data sets for each value of neutral density (ND) filter used to reduce signal strength in a controlled manner. Each recorded data set contained approximately 500 64PPM symbols, of which 10 consecutive symbols with a pulse in the first slot formed a preamble to help locate the beginning of the PPM data set. The same PPM data pattern was repeated at the transmitter continuously and recorded separately to facilitate the determination of symbol-error probability. The recorded PPM data were processed off-line to determine symbol-error probabilities of the individual telescopes and of the combined samples. Figure 9 shows experimental symbol-error probabilities for each telescope as well as for the combined signal, as a function of the total number of received signal photons.
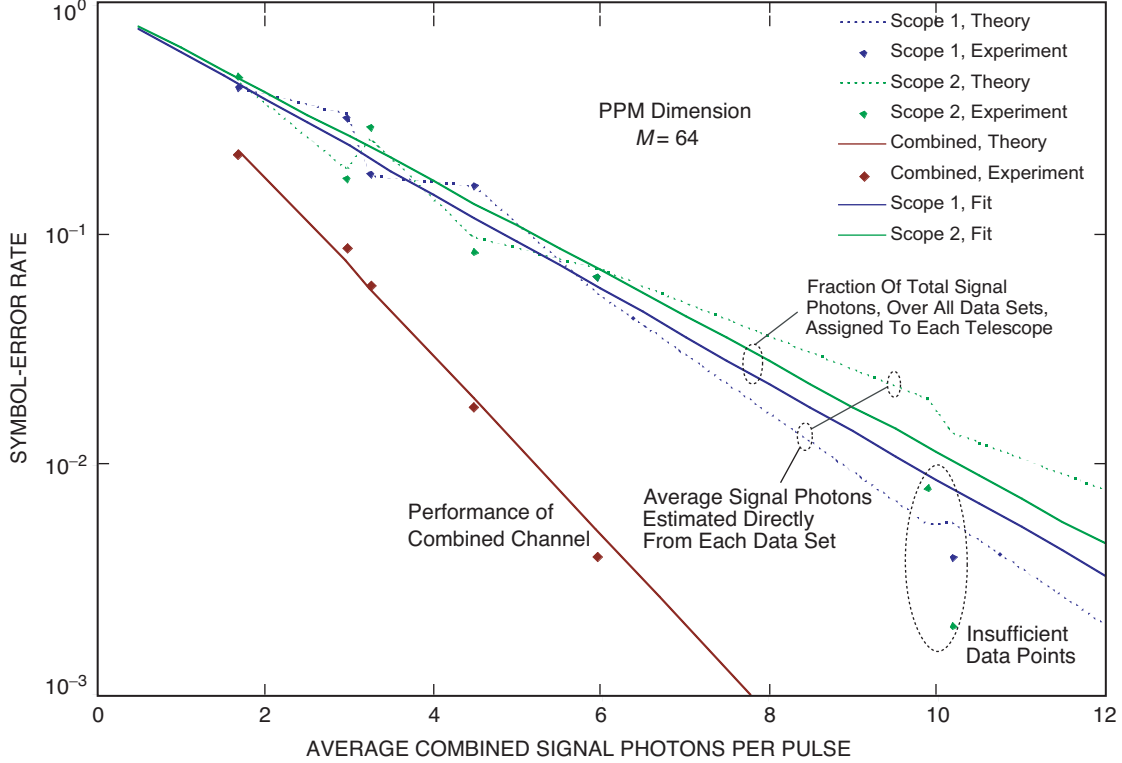
Fig. 9. Symbol-error rate for combined array channel, and for individual telescopes, demonstrating approximately a 3-dB array combining gain for a two-element array.

The process for calculating the PPM symbol-error rates (SERs) from each data set, for both individual and combined telescopes, began with synchronizing the received PPM symbol sequence with the transmitted sequence using the 10-symbol preamble. This provided both symbol and slot timing, so that slot statistics could be formed by summing the samples over each slot. The locations of the maximum slot counts then were compared with the known transmitted signal slot locations to calculate the experimental symbol-error rate. The known signal and background slot locations also were utilized to compute the mean noise slot count, which was used as an estimate of the average background photon count per slot, $K_b = \lambda_b \tau$, where λ_b is the average photon detection rate due to background and τ is the slot duration. The average background rates were subtracted from the mean signal-plus-background slot values to obtain an estimate of the average signal photon per pulse, $K_s = \lambda_s \tau$ (λ_s is the average photon detection rate due to the signal). These quantities then were used to calculate the theoretical PPM symbol-error rate. The received symbol is decoded correctly if the sum of the photon counts from all detector elements of the focal-plane array (FPA) over the signal-plus-noise slot exceeds the sum of photon counts over the FPA for every noise-only slot. Taking into account equal maximum counts among some or all of the slots (and resolving the ambiguity by a random choice among the maximal slots), the probability of correct detection can be expressed as

$$
P_M(C) = \left\{ \sum_{r=0}^{M-1} \left(\frac{1}{r+1} \right) \binom{M-1}{r} \sum_{k=1}^{\infty} \frac{(\lambda_s \tau + \lambda_b \tau)^k}{k!} e^{-(\lambda_s \tau + \lambda_b \tau)} \left[\frac{(\lambda_b \tau)^k}{k!} e^{-\lambda_b \tau} \right]^r \right.
$$

$$
\left. \times \left[\sum_{j=0}^{k-1} \frac{(\lambda_b \tau)^j}{j!} e^{-\lambda_b \tau} \right]^{M-1-r} \right\} + M^{-1} e^{-(\lambda_s + M\lambda_b)\tau}
$$

12

where M is the dimension of the PPM signal set. The last expression is the probability of making a correct detection if zero counts are observed in all of the PPM slots; this occurs with probability $e^{-(\lambda_s + M\lambda_b)\tau}$. When no counts are observed in any of the PPM slots, a random choice is made among the M possibilities, resulting in a correct decision with probability M^{-1}. The expression in brackets is the probability of correct detection when one or more counts are recorded, accounting for the number of ways ties can occur with the count in the signal slot among the remaining $M-1$ noise slots; in each case, a random choice is made to resolve ties among maximal counts. The corresponding symbol-error probability is given by $P_M(E) = 1 - P_M(C)$.

Theoretical Poisson symbol-error probabilities shown in Fig. 9 were calculated using two different approaches: First, the parameters for the mean number of signal and background photons were estimated from each data set, resulting in the dashed green and blue line segments for the individual telescopes; and second, the fraction of photons collected by each telescope over all data sets was computed, and the corresponding fraction of the combined photon count was assigned to each telescope. The dashed line segments follow small intensity variations between data sets in each telescope due to minor mechanical vibrations, and they yield excellent agreement with the experimentally determined SERs for each data set. The averaged SER generates a smoother theoretical curve, but since the short-term intensity variations between data sets have been averaged out, the apparent scatter of the experimental points with respect to the "averaged" theoretical curves is greater. It can be seen in Fig. 9 that the combined experimental symbol-error rates correspond very well with theory, validating the Poisson channel model and demonstrating optical array reception in the photon-counting regime. It is also evident that an array combining gain of approximately 3 dB was achieved, confirming the expected gain for a two-telescope array employing photon-counting detection and operating in the low-background regime.

III. Conclusions

Large-aperture optical receivers are difficult to construct and maintain, require massive support structures and drive assemblies, and represent a single point of failure in an optical communications system. Once constructed, the collecting area of a single large telescope cannot easily be expanded to meet future demands for enhanced performance. An array of small telescopes, on the other hand, provides a robust, scalable, parallel receiver architecture that can easily be expanded to accommodate higher data rates or greater distances.

A two-telescope optical array has been constructed using cost-effective 63.5-cm computer-controlled telescopes and a wide-field digital camera designed for the amateur market, together with high-speed photon-counting GAPD detector arrays equipped with digital signal-conditioning electronics, high-speed signal distribution and cable assemblies, and digital adaptive delay-compensation and combining electronics. The acquisition and tracking capabilities of the telescopes were evaluated in the field under realistic daytime operating conditions and found to have adequate mechanical accuracy when a star-hopping strategy was employed, but they would require increased mechanical rigidity and reduced backlash in the gears to satisfy the more stringent requirements of fully autonomous array operation.

Real-time array combining of photon counts generated by PPM laser pulses was demonstrated in the field using the high-speed digital electronics developed during this effort. However, due to bandwidth limitations of the available laser transmitter and modulator assemblies, only microsecond transmitted pulses could be used for this experiment instead of the much narrower 8-ns pulses the high-speed electronics were capable of generating. Photon counts generated by each telescope and real-time combined counts generated by the ADCCA were recorded and processed off-line to determine array detection performance. Excellent agreement with theory was obtained, demonstrating the 3-dB theoretical gain of the two-element array over either telescope operating alone. The results obtained during these field experiments indicate that an optical array receiver concept represents a viable alternative to the conventional single large-aperture approach for the reception of weak optical signals, with inherently greater design flexibility and resistance to single-point failure.

Acknowledgments

References

[1] V. Vilnrotter, C.-W. Lau, M. Srinivasan, R. Mukai, and K. Andrews, "Optical Array Receiver for Communication through Atmospheric Turbulence," *IEEE Journal of Lightwave Technology*, vol. 23, no. 4, pp. 1664–1675, April 2005.

[2] V. Vilnrotter, C.-W. Lau, K. Andrews, and M. Srinivasan, "Two-Element Optical Array Receiver Concept Demonstration," *The Interplanetary Network Progress Report*, vol. 42-161, Jet Propulsion Laboratory, Pasadena, California, pp. 1–20, May 15, 2005. http://ipnpr/progress_report/42-161/161K.pdf

[3] V. Vilnrotter, C.-W. Lau, M. Srinivasan, K. Andrews, and A. Portillo, "Two-Element Optical Array Receiver Development: Experimental Results," *Proceedings of SPIE, Free-Space Laser Communications Technologies XVII*, January 2005.

[4] C.-W. Lau, V. Vilnrotter, and M. Srinivasan, "Adaptive Delay Compensation Algorithms for the Optical Array Receiver," *The Interplanetary Network Progress Report*, vol. 42-161, Jet Propulsion Laboratory, Pasadena, California, pp. 1–10, May 15, 2005. http://ipnpr/progress_report/42-161/161E.pdf

[5] J. G. Proakis, *Digital Communications*, 4th edition, New York: McGraw-Hill, 1983.